

1 **Tradeoff between more cells and higher read depth for single-cell RNA-seq**  
2 **spatial ordering analysis of the liver lobule**

3  
4 Morten Seirup<sup>1,2\*</sup>, Li-Fang Chu<sup>2</sup>, Sri Kumar Sengupta<sup>2</sup>, Ning Leng<sup>2,3,#a</sup>, Christina M.  
5 Shafer<sup>2</sup>, Bret Duffin<sup>2</sup>, Angela L. Elwell<sup>2,#b</sup>, Jennifer M. Bolin<sup>2</sup>, Scott Swanson<sup>2</sup>, Ron  
6 Stewart<sup>2</sup>, Christina Kendzierski<sup>3</sup>, James A. Thomson<sup>2,4,5\*</sup>, Rhonda Bacher<sup>6,\*</sup>

7  
8 <sup>1</sup>Molecular and Environmental Toxicology Program, University of Wisconsin Madison,  
9 Madison, Wisconsin, United States of America

10 <sup>2</sup>Morgridge Institute for Research, Madison, Wisconsin, United States of America

11 <sup>3</sup>Department of Biostatistics and Medical Informatics, University of Wisconsin Madison,  
12 Madison, Wisconsin, United States of America

13 <sup>4</sup>Department of Cell & Regenerative Biology, University of Wisconsin School of Medicine  
14 and Public Health, Madison, Wisconsin, United States of America

15 <sup>5</sup>Department of Molecular, Cellular, & Developmental Biology, University of California  
16 Santa Barbara, Santa Barbara, California, United States of America

17 <sup>6</sup>Department of Biostatistics, University of Florida, Gainesville, Florida, United States of  
18 America

19 <sup>#a</sup>Current Address: Genentech, San Francisco, California, United States of America

20 <sup>#b</sup>Current Address: Department of Genetics, University of North Carolina at Chapel Hill,  
21 Chapel Hill, North Carolina, United States of America

22  
23 **\*Corresponding Authors:**

24 **Morten Seirup**

25 **E-mail: [seirup@wisc.edu](mailto:seirup@wisc.edu)**

26 **James A. Thomson, V.M.D., Ph.D., Diplomate A.C.V.P.**

27 **E-mail: [jthomson@morgridgeinstitute.org](mailto:jthomson@morgridgeinstitute.org)**

28 **Rhonda Bacher, Ph.D.**

29 **E-mail: [rbacher@ufl.edu](mailto:rbacher@ufl.edu)**

30

31

32

33

34

35

36

37

38

39

40

41

42 **Abstract**

43 As single-cell experiments generate increasingly more cells at reduced sequencing  
44 depths, the value of a higher read depth may be overlooked. Using data from two  
45 contrasting single-cell RNA-seq protocols that lend themselves to having either higher  
46 read depth (Smart-seq) or many cells (MARS-seq) we evaluate the trade-offs in the  
47 context of pseudo-spatial reconstruction of the liver lobule. Overall, we find gene  
48 expression profiles after spatial-reconstruction analysis are highly reproducible between  
49 datasets. Smart-seq's higher sensitivity and read-depth allows analysis of lower  
50 expressed genes and isoforms. Our analysis emphasizes the importance of selecting a  
51 protocol based on the biological questions and features of interest. Additionally, we  
52 evaluate trade-offs for each protocol by performing subsampling analyses, and find that  
53 optimizing the balance between sequencing depth and number of cells within a protocol  
54 is important for efficient use of resources.

55

56 **Introduction**

57 Single-cell RNA sequencing (scRNA-seq)<sup>1-5</sup> is a powerful tool for studying  
58 transcriptional differences between individual cells. The innovation of droplet-based  
59 techniques<sup>6,7</sup> and unique molecular identifiers (UMI)<sup>8</sup> has lowered the cost per cell and  
60 pushed the field towards obtaining data from tens of thousands of cells per experiment  
61 albeit at a reduced sequencing depth. Recent publications have compared the  
62 sensitivity, accuracy, and precision between several scRNA-seq techniques and report  
63 the major trade-off between protocols is sensitivity, which is dependent on read  
64 depth<sup>9,10</sup>. With the push for sequencing an ever-increasing number of cells at the  
65 expense of read depth per cell, the value of a higher read depth might be overlooked.  
66 Here we investigate the trade-off of more cells versus higher read depth in the context  
67 of pseudo-spatial reconstruction by comparing two independently produced scRNA-seq  
68 datasets on mouse liver lobule, one using Smart-seq<sup>2</sup>--a full-length protocol and one

69 using MARS-seq<sup>11</sup>--a UMI based protocol. Although the cell number and read depth  
70 differ greatly, we find high reproducibility between protocols of gene expression profiles  
71 after spatial-reconstruction analysis. We find that the increased read depth of the Smart-  
72 seq protocol enables studies of lower expressed genes and isoforms of genes. Our  
73 results demonstrate the importance of carefully evaluating the biological question and  
74 features of interest when selecting the appropriate sequencing protocol. In applications  
75 focused on lower expressed genes or on genes with high sequence similarity, increased  
76 read depth is preferable, whereas a focus on identifying cell types based on more highly  
77 expressed genes will benefit from collecting more cells. In an ideal situation a single cell  
78 assay would result in thousands of cells that are all sequenced at a high read depth, but  
79 technical and financial restrictions make this rarely possible.

80 Studies comparing protocols have mainly done so with respect to performance  
81 on spike-ins or on technical variability alone<sup>9,10</sup>. Recently, Guo et al.<sup>12</sup> showed  
82 agreement of cell types and signature genes between two protocols used for single-cell  
83 RNA-seq for Fluidigm C1 and Drop-seq. However, few studies have examined  
84 comparative agreement among protocols for biological inferences beyond clustering  
85 and identifying differential gene expression, and a key question of interest with single-  
86 cell data is its ability to reflect temporal or spatial heterogeneity. For cells collected at a  
87 given time, the underlying dynamic biological process is reflected in genome-wide  
88 differences in gene expression. Computational algorithms that attempt to order cells in  
89 pseudo-time or pseudo-space based on variability in gene expression have been  
90 developed<sup>4,13,14</sup>, and more than 45 existing algorithms were recently compared<sup>15</sup>. Yet,

91 as far as we know, no comparison of single-cell protocols exists for the question of cell  
92 ordering.

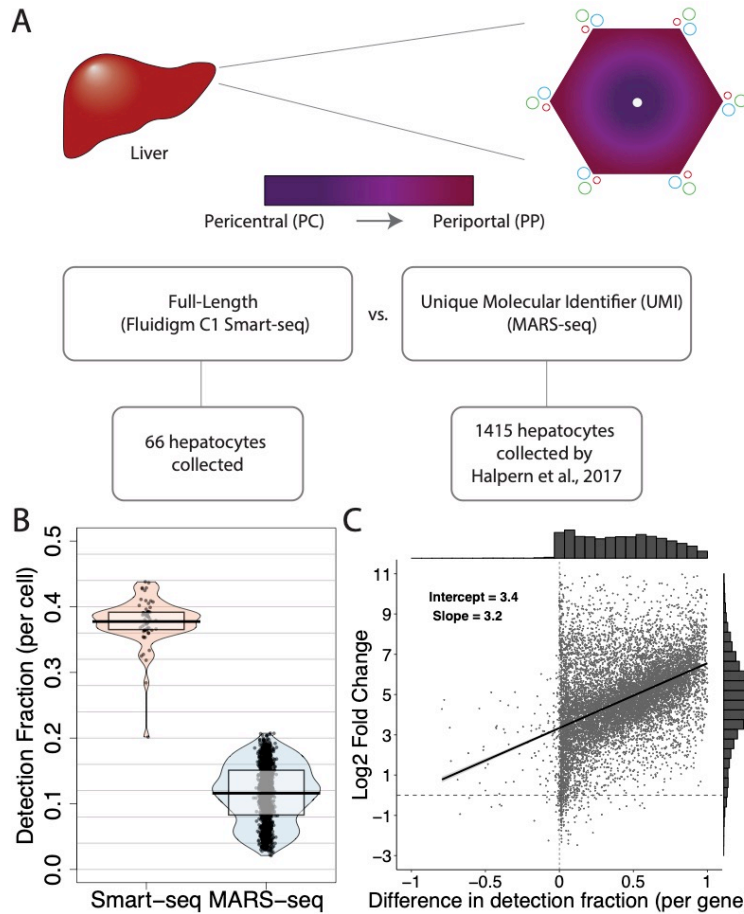
93 Here, we chose to compare protocols on their ability to reflect the spatial  
94 patterning of the liver lobule. The main functional cells of the liver, hepatocytes, are  
95 organized spatially in a polygonal shape around a central vein (Figure 1A). From the  
96 central vein, a gradient of metabolic functions is performed extending to a portal vein at  
97 each vertex<sup>16–20</sup>. The gradient of differences in gene expression patterns is referred to  
98 as the zonation axis (from periportal (PP) to pericentral (PC))<sup>21</sup>. This coordinated spatial  
99 organization provides a particularly interesting application of single-cell techniques. For  
100 this study we obtained scRNA-seq data from 66 hepatocytes using the Fluidigm C1  
101 system with the Smart-seq full-length protocol, and compare this dataset at the gene  
102 level to a dataset collected by Halpern et al. 2017 containing 1415 hepatocytes using  
103 the MARS-seq protocol with UMI's<sup>22</sup> (Figure 1A). We compare the ability of these two  
104 single-cell datasets to spatially resolve the zonation axis of the liver.

105

## 106 **Results**

107 By using the Fluidigm C1 coupled with the Smart-seq protocol, we were able  
108 identify on average around 38% (about 7100 genes) (Figure 1B) of all genes in the  
109 genome expressed per cell, whereas the MARS-seq dataset finds on average 12%  
110 (about 2100 genes) (Figure 1B) of all genes in the genome expressed per cell. This is in  
111 accordance with what was found by Ziegenhain et al. 2017 when they examined the  
112 methods, and underscores the increased sensitivity of the Fluidigm C1/SMART-seq  
113 protocol over MARS-seq<sup>9</sup>. This increased sensitivity is further illustrated in Figure 1C,

114 which on a per gene level shows the difference in detection fraction compared to the log  
115 fold change in mean expression between the two protocols. A difference in detection  
116 fraction of zero means that the gene is detected in the same fraction of cells in both  
117 datasets and a positive value is the result of a gene detected in a larger fraction of cells  
118 in the Smart-seq protocol compared to the MARS-seq protocol, and a negative value  
119 corresponds to the opposite case where the MARS-seq protocol detects the gene in a  
120 higher fraction of cells. The difference across protocols in log2 fold-change has a linear  
121 relationship with the difference in detection fractions, which indicates a fairly constant  
122 increase in log2 expression expected as cells are sequenced with greater sensitivity. At  
123 the intercept, a difference in detection equal to zero, the log2 fold change is 3.4,  
124 indicating an experiment wide increase in sensitivity in the Smart-seq protocol of  
125 approximately 10-fold. In fact, the vast majority of genes are detected in a larger fraction  
126 of cells (positive value on the x-axis) and have a higher expression level (positive value  
127 in the y-axis) sequenced using Smart-seq protocol. Although, it is worth pointing out that  
128 around 6% of genes have higher detection using the MARS-seq protocol (negative  
129 values on x-axis) and a few of these genes also have higher expression levels (negative  
130 values on y-axis) than in the Smart-seq protocol. The subset of genes better detected in  
131 the MARS-seq dataset have higher GC content and are slightly longer (Supplementary  
132 Figure 1), which is consistent with previous reports of protocol comparisons<sup>23,24</sup>.



133

134 Figure 1. Illustration of the liver anatomy, and general comparison of the datasets.

135 A) Top. Illustration of the liver lobule identifying the portal triad along the outer edges

136 and the central vein in the middle. The color gradient represents metabolic zonation. A)

137 Bottom. Highlights the main differences between the datasets compared. B)

138 Comparison of gene detection fraction between the datasets. The detection fraction per

139 cell (y-axis) is shown for the two datasets (x-axis). C) The log2 fold-change of genes

140 detected above an average expression level of zero in the Smart-seq dataset compared

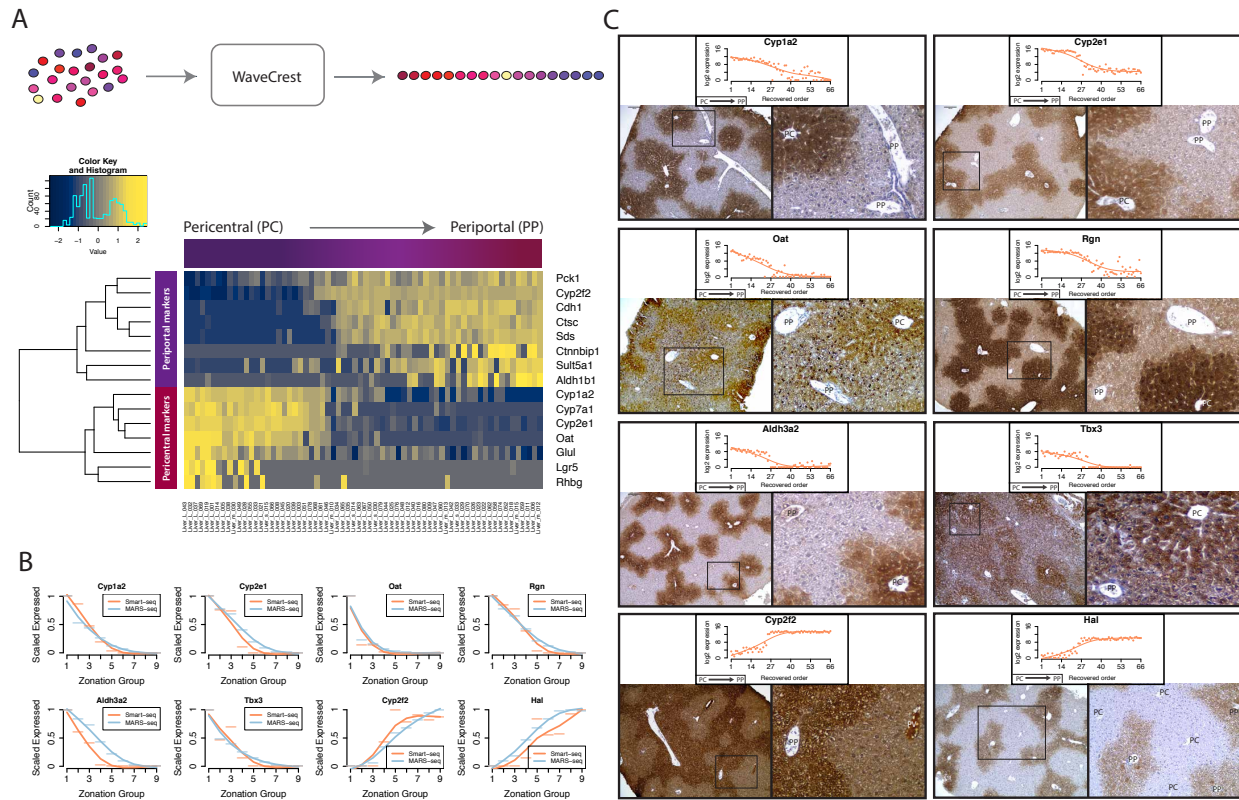
141 to the MARS-seq dataset (y-axis), versus the difference in gene-level detection fractions

142 across datasets (x-axis). A linear regression line is overlaid and a histogram of the x-

143 and y-axis are shown opposite of each axis.

144

145 Next, to represent the spatial patterns across the liver lobule, the cells in the two  
146 datasets were computationally ordered according to their expression profiles. The  
147 MARS-seq dataset was spatially ordered by Halpern et al. 2017 by first performing  
148 smFISH for six marker genes at various locations across the zonation axis, then single-  
149 cell RNA-seq data obtained by MARS-seq were assigned into one of nine zonation  
150 locations based on each cell's expression profile of the six marker genes<sup>22</sup>. For the  
151 Smart-seq protocol we used a computational algorithm called Wave-Crest to spatially  
152 order the 66 cells along the zonation axis (Figure 2A)<sup>5</sup>. The ordering is based on fifteen  
153 marker genes known in the literature to be differentially expressed along the zonation  
154 axis. Cells were ordered using the nearest insertion algorithm implemented in the  
155 Wave-Crest package. The algorithm searches among the space of all possible  
156 orderings via a 2-opt algorithm by considering insertion events and choosing orders  
157 which minimize the mean square error of a polynomial regression on the marker genes  
158 expression. Of the 15 genes used, we selected eight periportal expressed genes and  
159 seven pericentral expressed genes<sup>21</sup>. Both orderings assume the zonation profile and  
160 spatial organization can be represented in a single dimension.



161

162 **Figure 2. Pseudo-space reordering of hepatocytes, and prediction and validation of**  
163 **dynamically expressed genes. A) Top. Illustration of the pseudo-spatial reordering of the**  
164 **Smart-seq experiment. Bottom. Heatmap showing the pseudo-spatial reordering (x-axis)**  
165 **and the expression levels of the marker genes (y-axis) for the Smart-seq dataset.**  
166 **Pericentral cells are found on the left-hand side and Periportal cells are found on the**  
167 **right-hand side. B) Scaled expression profile (y-axis) of 8 dynamic genes based on the**  
168 **predicted pseudo-space reordering (x-axis) of the Smart-seq dataset (orange), and the**  
169 **MARS-seq dataset (blue). C) Immunohistochemistry staining of the genes highlighted in**  
170 **B). Above the staining is the predicted log2 expression levels (y-axis) across the**  
171 **pseudo-spatial order (x-axis). The left picture shows the staining and the right picture is**  
172 **an enlarged section (black square). PP = Periportal, PC = Pericentral.**

173

174           Using the recreated order of the hepatocytes we explored dynamic gene  
175    expression across the periportal to pericentral axis. Figure 2B shows a subset of genes  
176    that are predicted to be highly regulated across the axis, four of which were not in our  
177    list of marker genes. We first compared their expression across the zonation axis in the  
178    Smart-seq dataset to that from the MARS-seq dataset. Since the MARS-seq dataset  
179    placed cells into nine discrete zones along the axis, we divided cells from the Smart-seq  
180    dataset into nine equally sized groups. The zonation profiles in Figure 2B have high  
181    agreement, with a median Spearman correlation of 0.93. Before proceeding, we also  
182    performed an additional experiment to validate that our cell ordering and expression  
183    profiles reflect those of the liver lobule *in vivo*. Immunohistochemistry was performed on  
184    sections of paraffin embedded livers with antibodies against select genes from either  
185    category (Figure 2C). A complete list of dynamic genes across the zonation axis from  
186    the Smart-seq dataset is provided in Additional File 2, and scatter plots are in Additional  
187    File 3.

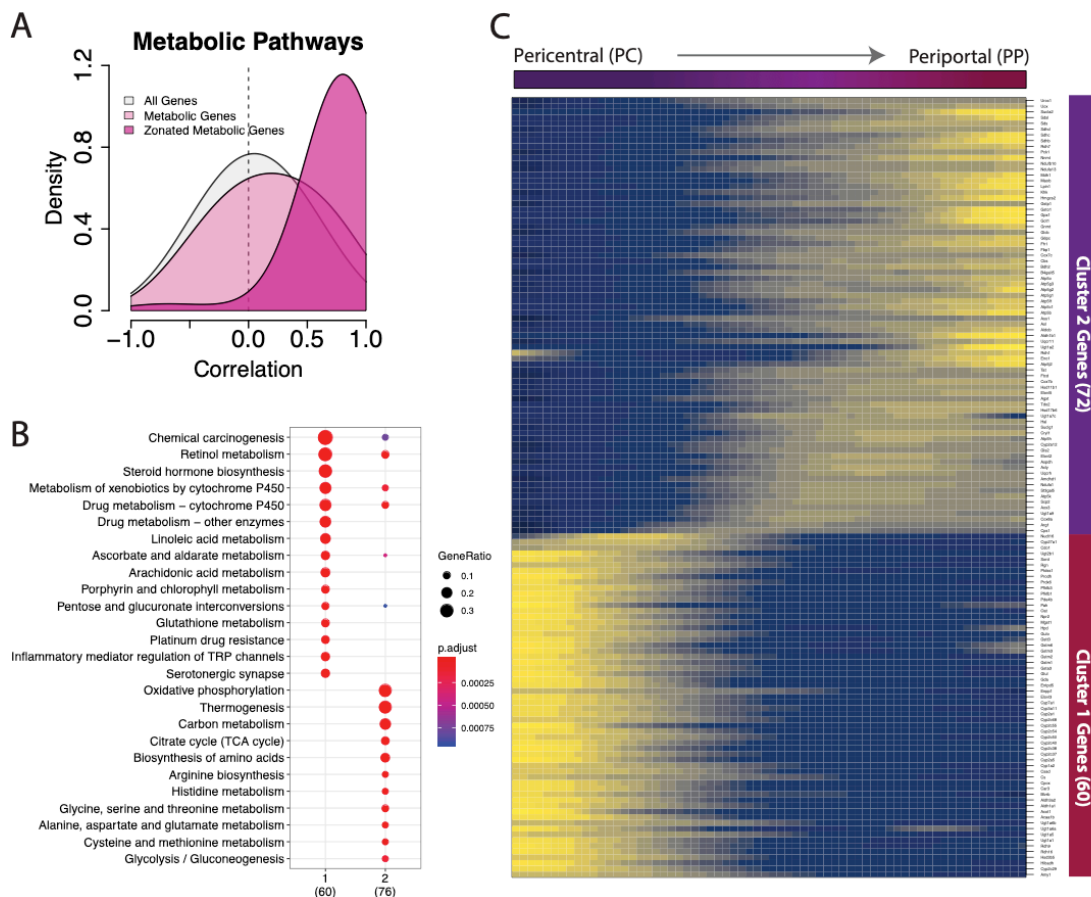
188           An exciting prospect of single cell analysis is the identification of genes that have  
189    non-monotonic or dynamic expression along the liver lobule. Several genes in the bile  
190    acid synthesis pathway was shown by Halpern et al. to be non-monotonically expressed  
191    in a pattern where the highest expression levels along the lobule corresponds to the  
192    functional placement of the genes in the bile acid synthesis pathway (Cyp7a1, Hsd3b7,  
193    Cyp8b1, Cyp27a1 and Baat). We find that the expression profiles for these genes,  
194    besides Cyp8b1, found in the Smart-seq dataset match the patterns found in the MARS-  
195    seq dataset (Supplementary Figure 3A). In the Smart-seq dataset, Cyp8b1 is found to  
196    have largely flat expression levels along most of the lobule and lower expression toward

197 the periportal zone. Other genes shown to be non-monotonically expressed such as  
198 Hamp, Igfbp2 and Mup3 in Halpern et al. were also identified to be non-monotonically  
199 expressed in the Smart-seq dataset (Supplementary Figure 3B). The ability to identify  
200 gene expression profiles that are either high at the PP end, high at the PC end or high  
201 in the middle of the liver lobule confirms that the sampling depth is sufficient to spatially  
202 reconstruct the liver lobule. We also investigated the expression pattern of Glul in more  
203 detail as it is known to be expressed highly in a one hepatocyte wide band around the  
204 central vein<sup>25</sup>. Accordingly, the predicted expression pattern found using the Smart-seq  
205 dataset demonstrated sufficient sampling of this region (Supplementary Figure 3C).

206 We further compared the zonation profiles between datasets and found a high  
207 correlation of gene expression and spatial location of transcripts across the periportal to  
208 pericentral axis. For genes significantly zonated in both datasets (having adjusted p-  
209 value < .1) the median Spearman correlation is 0.73. In Figure 3A we looked at zonated  
210 genes within the metabolic pathways in KEGG, and found the median correlation  
211 between datasets (highlighted in dark pink) is 0.82. Among all genes in that pathway  
212 (light pink) the correlation is moderate with a median of 0.18, and no correlation is found  
213 when all genes are considered (grey).

214 Traditionally the liver lobule is divided into three zones, a periportal zone 1, a  
215 pericentral zone 3 and transitioning zone 2<sup>26,27</sup>. The transitional nature of the liver axis is  
216 reflected in the heatmap of metabolic genes that were significantly zonated in both  
217 datasets (Figure 3B). Using k-means clustering, we found the Smart-seq data tended to  
218 cluster into two distinct gene groups representing either the periportal or pericentral  
219 zone. Examination of the two clusters by enrichment analysis of KEGG metabolic

220 pathways (Figure 3C) revealed that the predicted location along our reconstructed axis  
221 of metabolic processes with known periportal or pericentral bias such as amino acid  
222 metabolism (periportal), lipogenesis (pericentral) and CYP450 metabolism (pericentral)  
223 corresponds to their known *in vivo* locations<sup>27</sup>. Despite using different reordering  
224 algorithms and protocols, the two datasets show high agreement of expression along  
225 the recovered pericentral to periportal axis among genes that are detectable in both  
226 datasets, and both reliably mirror the *in vivo* patterning of the liver lobule (additional  
227 KEGG categories are shown in Supplementary Figure 2).

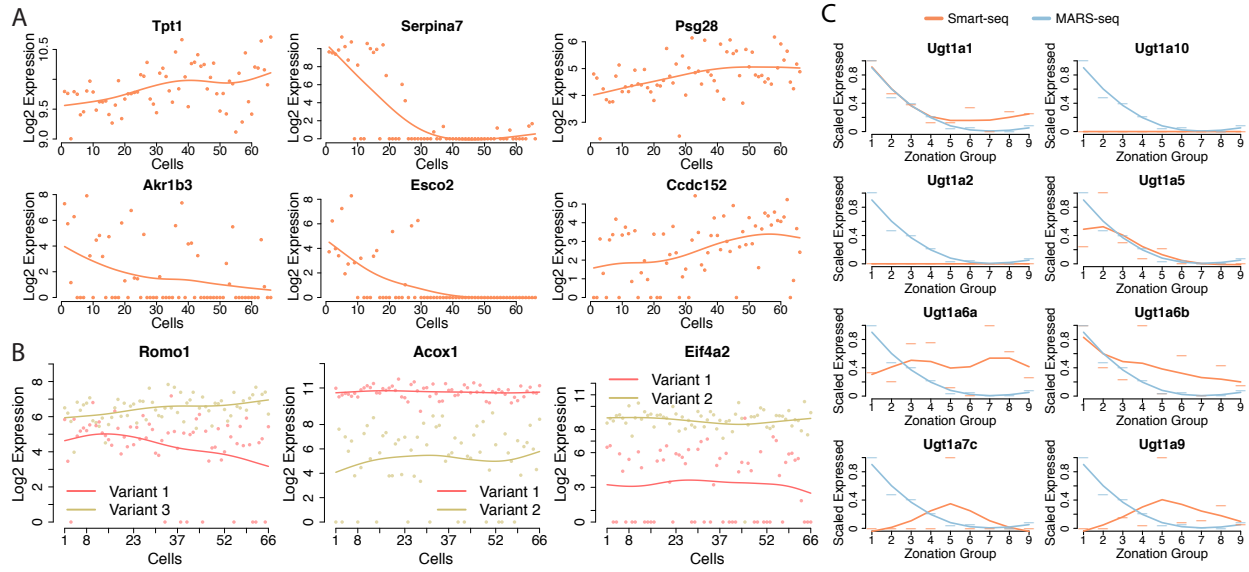


228  
229 Figure 3. Correlation and Gene Ontology analysis of genes between datasets.  
230 A) Correlation analysis of genes annotated to the metabolic pathways in KEGG  
231 between the datasets. The dark pink density is the correlation of genes from the

232 metabolic pathways with significant zonation profiles in both datasets. The light pink  
233 density displays the correlation of all genes in the metabolic pathway and the grey  
234 density displays the correlation of all genes. B) Heatmap of the expression level of  
235 genes that are significantly differentially zonated in both datasets and enriched in the  
236 metabolic KEGG pathway. C) Breakdown of KEGG enrichment analysis of the two k-  
237 mean clusters based on the genes shown in B. Dot size represents the fraction of  
238 enriched genes in each ontology, and the color represents the adjusted p-value for the  
239 enrichment.

240

241 When we look at genes with moderate and low expression levels, we find that the  
242 two datasets differ to a greater degree. We identified twenty genes that were classified  
243 as significantly zonated along the periportal to pericentral axis in the Smart-seq dataset  
244 that were not detected at all in the MARS-seq dataset, whereas only three such genes  
245 were exclusive to the MARS-seq dataset. Figure 4A shows six most highly expressed  
246 genes that we were able to exclusively identify in the Smart-seq dataset having  
247 significant zonation (adjusted p-value < 0.10). This is not a surprising result due to the  
248 well-known sensitivity advantage the C1/Smart-seq technique holds over the MARS-seq  
249 technique.



250

251 Figure 4. Genes and isoforms found in the full-length dataset and not in the UMI  
252 dataset. A) Six genes found to be zonally expressed in the Smart-seq dataset that were  
253 not detected in the MARS-seq dataset. The log2 of expression values are represented  
254 on the y-axis and the pseudo-space ordered cells are found on the x-axis. B) Examples  
255 of genes with two transcript variants expressed differently across reordered cells from  
256 the Smart-seq dataset. C) Eight Ugt1a genes that were concatenated in the MARS-seq  
257 dataset (blue on all graphs), but can be resolved in the Smart-seq dataset (orange line).

258

259 Further, an exciting field of study that benefits from an enhanced resolution of  
260 scRNA-seq is isoform analysis<sup>28-30</sup>. Many genes in the genome have two or more  
261 isoforms that are distinctly expressed and can change properties such as structure,  
262 function and localization of the resulting protein<sup>31</sup>. Due to the increased sensitivity of the  
263 C1/Smart-seq protocol compared to MARS-seq we were able to examine genes with  
264 known isoforms, and identify cases where the transcript variants for each isoform has  
265 distinct expression from each other across the periportal to pericentral axis, which is not

266 possible with less sensitive protocols. In Figure 4B the transcript variants of Romo1 are  
267 seen to display opposite trends in expression across the zonation axis, where the  
268 Romo1 variant 3 is increasing in expression from the pericentral end towards the  
269 periportal end and the Romo1 variant 1 is decreasing in expression along the same  
270 axis. We also highlight genes Acox1 and Eif4a2 whose variants both show constant  
271 expression across the zonation axis but at different levels. Both of these genes are  
272 known to have isoform specific expression in the liver lobule<sup>32,33</sup>. (For Ensembl and  
273 ENTREZ IDs for transcript variants see Supplementary Table 1).

274 We also note that due to the nature of the MARS-seq protocol there is also an  
275 inability to resolve not just isoforms but many genes that are closely related. There were  
276 242 concatenated genes in the MARS-seq set corresponding to 539 unique genes. An  
277 example of this is seen in Figure 4C where we highlight a concatenate of Ugt1a  
278 enzymes as another example of this. Eight genes are concatenated and when  
279 combined the average expression level is shown to be high at the pericentral end of the  
280 lobule and low at the periportal end. Again, it is clear that not all the members of this  
281 concatenated group follow this trend and Ugt1a6a can be seen to have consistent  
282 expression levels across the pericentral to periportal axis.

283 To further study the trade-offs between higher depth versus more cells, we  
284 performed a subsampling experiment. For each dataset, we held either the number of  
285 cells or the sequencing depth constant while varying the other. For the Smart-seq  
286 dataset, we evaluated the effect on the cell ordering as well as the gene-specific  
287 zonation profiles. For the MARS-seq dataset, the assignment of each cell to a zonation  
288 group depended on external data and was independent of the other cells profiled, thus

289 we only evaluated the effect on zonation profiles. In Supplementary Figure 4A&B, the  
290 MARS-seq dataset displayed an approximately linear tradeoff in zonation profile error  
291 for fewer cells at the original read depth. While, at reduced read depth using the original  
292 1,415 cells, a linear increase in error only existed up to 70% of the total depth, and at  
293 lower levels the error increased exponentially. The average mean squared error we  
294 observed in zonation profiles through subsampling in the MARS-seq dataset indicates  
295 that resequencing at the same depth results in error that is equivalent to reducing the  
296 total cells by about 400. Thus, in scenarios with such low sequencing depth (average of  
297 11.7k total UMIs per cell), sequencing deeper would be more beneficial than adding  
298 more cells. For the Smart-seq dataset, we found the spatial ordering to be quite robust  
299 to reduced sequencing depth, even as low as 50% fewer reads and only marginal  
300 increases in gene-specific zonation error as shown in Supplementary Figure 4C&D. The  
301 average sequencing depth for the Smart-seq cells was 3.5 million counts per cell, well  
302 beyond the commonly suggested sequencing saturation for single-cell data that occurs  
303 close to one million total reads<sup>34</sup>. We do see more significant increases in error related  
304 to zonation profiles when profiling fewer cells in Supplementary Figure 4E. Here the  
305 tradeoff of sequencing to even half of the current depth and increasing the number of  
306 cells would be beneficial.

307

## 308 **Discussion**

309 In summary, we compared two scRNA-seq datasets of mouse hepatocytes  
310 where one, MARS-seq, is wide but shallow (1500 cells and about 3000 genes per cell)  
311 and the other, C1/Smart-seq is narrow but deep (66 cells and 8000 genes per cell). We

312 find that the two different protocols present highly reproducible liver zonation profiles in  
313 single cells, and for the vast majority of genes that are highly expressed we observe  
314 highly comparable results. We do however find that when we look at medium to low  
315 expressed genes the increased sensitivity of the C1/Smart-seq protocol is able to  
316 identify several genes exclusive to this dataset. This increased sensitivity also allowed  
317 us to identify several genes with isoforms that behaved differently across the periportal  
318 to pericentral axis. We are aware of the limitation of short reads in regard to isoform  
319 analysis and if more accuracy is needed, the newly developed technique ScISOr-seq<sup>35</sup>  
320 might be better suited. We do however believe that this data allows for preliminary  
321 isoform analysis. We were able to resolve and identify individual genes with differing  
322 spatial patterns that lower sensitivity techniques are unable to distinguish. The main  
323 weakness of using fewer cells is that it is less likely that rare cell types will be sampled.  
324 In cases where such rare cells are of high interest, protocols that produce a large  
325 number of cells are preferable. In an ideal case, one would sample many cells and  
326 sequence all of them deeply, unfortunately, this is not always possible in practice and  
327 the decision of whether to sample many cells shallowly or fewer cells deeply comes  
328 down to whether rare cell types are of interest or if higher resolution of the individual  
329 cells is preferred. Given the distinct advantages, we emphasize that the biological  
330 question should be the driving factor when deciding on protocol. Within a chosen  
331 protocol, achieving balance between the sequencing depth and the number of cells is  
332 still an important consideration for optimal use of resources. Based on our simulations  
333 of two datasets at opposite ends of the sequencing depth versus number of cells trade-  
334 off, there is eventually a detriment to sacrificing reads for additional cells or sequencing

335 beyond the attainable sensitivity level on too few cells. We expect that the extent of the  
336 cells versus depth trade-off will vary for other cell types or tissues and it will largely  
337 depend on the heterogeneity of the biological system under study.

338

339 **Author contributions.**

340 Morten Seirup and James A. Thomson designed the experiments. Morten Seirup, Li-  
341 Fang Chu and Srikumar Sengupta performed the experiments. Angela L. Elwell, and  
342 Jennifer M. Bolin prepared sequencing libraries. Bret Duffin provided animal husbandry.  
343 Christina M. Shafer and Scott Swanson developed the sequencing and alignments  
344 pipeline. Rhonda Bacher performed statistical analyses (with input from Ron Stewart  
345 and Christina Kendziorski and Ning Leng). Morten Seirup, James A. Thomson and  
346 Rhonda Bacher supervised the project. Morten Seirup, James A. Thomson, and  
347 Rhonda Bacher wrote the paper. All authors read and approved the final manuscript.

348

349 **Competing interests.**

350 The authors declare that they have no competing interests

351  
352 **References.**

353

354 1. Tang, F. *et al.* mRNA-Seq whole-transcriptome analysis of a single cell. *Nat Methods* **6**,  
355 377–382 (2009).

356 2. Ransköld, D. *et al.* Full-length mRNA-Seq from single-cell levels of RNA and individual  
357 circulating tumor cells. *Nat Biotechnol* **30**, 777–782 (2012).

358 3. Islam, S. *et al.* Characterization of the single-cell transcriptional landscape by highly  
359 multiplex RNA-seq. *Genome Research* **21**, 1160–1167 (2011).

360 4. Leng, N. *et al.* Oscope identifies oscillatory genes in unsynchronized single-cell RNA-seq  
361 experiments. *Nat Methods* **12**, 947–950 (2015).

362 5. Chu, L.-F. *et al.* Single-cell RNA-seq reveals novel regulators of human embryonic stem cell  
363 differentiation to definitive endoderm. *Genome Biol* **17**, 173 (2016).

364 6. Klein, A. M. *et al.* Droplet Barcoding for Single-Cell Transcriptomics Applied to Embryonic  
365 Stem Cells. *Cell* **161**, 1187–1201 (2015).

366 7. Macosko, E. Z. *et al.* Highly Parallel Genome-wide Expression Profiling of Individual Cells  
367 Using Nanoliter Droplets. *Cell* **161**, 1202–1214 (2015).

368 8. Islam, S. *et al.* Quantitative single-cell RNA-seq with unique molecular identifiers. *Nat  
369 Methods* **11**, 163–166 (2014).

370 9. Ziegenhain, C. *et al.* Comparative Analysis of Single-Cell RNA Sequencing Methods.  
371 *Molecular Cell* **65**, 631-643.e4 (2017).

372 10. Svensson, V. *et al.* Power analysis of single-cell RNA-sequencing experiments. *Nat Methods*  
373 **14**, 381–387 (2017).

374 11. Jaitin, D. A. *et al.* Massively Parallel Single-Cell RNA-Seq for Marker-Free Decomposition  
375 of Tissues into Cell Types. *Science* **343**, 776–779 (2014).

376 12. Guo, M. *et al.* Single cell RNA analysis identifies cellular heterogeneity and adaptive  
377 responses of the lung at birth. *Nat Commun* **10**, 37 (2019).

378 13. Trapnell, C. *et al.* The dynamics and regulators of cell fate decisions are revealed by  
379 pseudotemporal ordering of single cells. *Nat Biotechnol* **32**, 381–386 (2014).

380 14. Ji, Z. & Ji, H. TSCAN: Pseudo-time reconstruction and evaluation in single-cell RNA-seq  
381 analysis. *Nucleic Acids Res* **44**, e117–e117 (2016).

382 15. Saelens, W., Cannoodt, R., Todorov, H. & Saeys, Y. A comparison of single-cell trajectory  
383 inference methods. *Nat Biotechnol* **37**, 547–554 (2019).

384 16. Burger, H.-J., Gebhardt, R., Mayer, C. & Mecke, D. Different capacities for amino acid  
385 transport in periportal and perivenous hepatocytes isolated by digitonin/collagenase  
386 perfusion. *Hepatology* **9**, 22–28 (1989).

387 17. Pösö, A. R., Penttilä, K. E., Suolinna, E. M. & Lindros, K. O. Urea synthesis in freshly  
388 isolated and in cultured periportal and perivenous hepatocytes. *Biochem. J.* **239**, 263–267  
389 (1986).

390 18. Tosh, D., Alberti, G. M. M. & Agius, L. Glucagon regulation of gluconeogenesis and  
391 ketogenesis in periportal and perivenous rat hepatocytes. Heterogeneity of hormone action  
392 and of the mitochondrial redox state. *Biochem. J.* **256**, 197–204 (1988).

393 19. Guzmán, M. & Castro, J. Zonation of fatty acid metabolism in rat liver. *Biochem. J.* **264**,  
394 107–113 (1989).

395 20. Anundi, I., Lähteenmäki, T., Rundgren, M., Moldeus, P. & Lindros, K. O. Zonation of  
396 acetaminophen metabolism and cytochrome P450 2E1-mediated toxicity studied in isolated  
397 periportal and perivenous hepatocytes. *Biochemical Pharmacology* **45**, 1251–1259 (1993).

398 21. Braeuning, A. *et al.* Differential gene expression in periportal and perivenous mouse  
399 hepatocytes. *FEBS Journal* **273**, 5051–5061 (2006).

400 22. Halpern, K. B. *et al.* Single-cell spatial reconstruction reveals global division of labour in the  
401 mammalian liver. *Nature* **542**, 352–356 (2017).

402 23. Parekh, S., Ziegenhain, C., Vieth, B., Enard, W. & Hellmann, I. The impact of amplification  
403 on differential expression analyses by RNA-seq. *Sci Rep* **6**, 25533 (2016).

404 24. Phipson, B., Zappia, L. & Oshlack, A. Gene length and detection bias in single cell RNA  
405 sequencing protocols. *F1000Res* **6**, 595 (2017).

406 25. Gebhardt, R. & Mecke, D. Heterogeneous distribution of glutamine synthetase among rat  
407 liver parenchymal cells in situ and in primary culture. *The EMBO Journal* **2**, 567–570  
408 (1983).

409 26. Bhatia, S. N. *et al.* Zonal liver cell heterogeneity: effects of oxygen on metabolic functions of  
410 hepatocytes. *Cell Eng* **1**, 125–135 (1996).

411 27. Kietzmann, T. Metabolic zonation of the liver: The oxygen gradient revisited. *Redox Biology*  
412 **11**, 622–630 (2017).

413 28. Song, Y. *et al.* Single-Cell Alternative Splicing Analysis with Expedition Reveals Splicing  
414 Dynamics during Neuron Differentiation. *Molecular Cell* **67**, 148-161.e5 (2017).

415 29. Karlsson, K., Lönnerberg, P. & Linnarsson, S. Alternative TSSs are co-regulated in single  
416 cells in the mouse brain. *Mol Syst Biol* **13**, 930 (2017).

417 30. Arzalluz-Luque, Á. & Conesa, A. Single-cell RNAseq for the study of isoforms—how is that  
418 possible? *Genome Biol* **19**, 110 (2018).

419 31. Wang, E. T. *et al.* Alternative isoform regulation in human tissue transcriptomes. *Nature*  
420 **456**, 470–476 (2008).

421 32. Gruppuso, P. A., Tsai, S.-W., Boylan, J. M. & Sanders, J. A. Hepatic translation control in  
422 the late-gestation fetal rat. *American Journal of Physiology-Regulatory, Integrative and*  
423 *Comparative Physiology* **295**, R558–R567 (2008).

424 33. Oaxaca-Castillo, D. *et al.* Biochemical characterization of two functional human liver acyl-  
425 CoA oxidase isoforms 1a and 1b encoded by a single gene. *Biochemical and Biophysical*  
426 *Research Communications* **360**, 314–319 (2007).

427 34. Haque, A., Engel, J., Teichmann, S. A. & Lönnberg, T. A practical guide to single-cell RNA-  
428 sequencing for biomedical research and clinical applications. *Genome Med* **9**, 75 (2017).

429 35. Gupta, I. *et al.* Single-cell isoform RNA sequencing characterizes isoforms in thousands of  
430 cerebellar cells. *Nat Biotechnol* **36**, 1197–1202 (2018).

431 36. Brennecke, P. *et al.* Accounting for technical noise in single-cell RNA-seq experiments. *Nat*  
432 *Methods* **10**, 1093–1095 (2013).

433 37. Langmead, B., Trapnell, C., Pop, M. & Salzberg, S. L. Ultrafast and memory-efficient  
434 alignment of short DNA sequences to the human genome. *Genome Biol* **10**, R25 (2009).

435 38. Li, B. & Dewey, C. N. RSEM: accurate transcript quantification from RNA-Seq data with or  
436 without a reference genome. *BMC Bioinformatics* **12**, 323 (2011).

437 39. Bacher, R. *et al.* SCnorm: robust normalization of single-cell RNA-seq data. *Nat Methods*  
438 **14**, 584–586 (2017).

439 40. Yu, G., Wang, L.-G., Han, Y. & He, Q.-Y. clusterProfiler: an R Package for Comparing  
440 Biological Themes Among Gene Clusters. *OMICS: A Journal of Integrative Biology* **16**,  
441 284–287 (2012).

442  
443 **Materials and Methods**  
444

445 **Animals and handling.**

446 All animals were kept under standard husbandry conditions. A wildtype 8-week-old male  
447 C57BL/6 (Jackson laboratories) was used in this experiment. Using isoflurane, the  
448 mouse was anesthetized before euthanizing by cervical dislocation. Animal experiments  
449 and procedures were approved by the University of Wisconsin Medical School's Animal

450 Care and Use Committee and conducted in accordance with the Animal Welfare Act  
451 and Health Research Extension Act.

452

453 **Cell isolation.**

454 The euthanized mouse was pinned to a Styrofoam plate using 20 ga needles to aid in  
455 dissection. The abdominal cavity was opened, and the portal vein exposed. A piece of  
456 4-0 suture thread (Ethicon vicryl coated) was threaded under the portal vein and used to  
457 secure a 26 ga catheter inserted into the portal vein (Butler Schein animal health 26 G  
458 IV Catheter, Fisher Scientific). Hepatocytes were isolated using a 2-step perfusion  
459 protocol. First, Liver Perfusion Medium (Gibco) warmed to 37°C was pumped through  
460 the catheter for 10 minutes using a peristaltic pump at 7 ml/min flowrate. Then, Liver  
461 Digest Medium (Gibco) warmed to 37°C was pumped through the liver at the same  
462 settings for 10 minutes. After perfusion, the liver was excised and transferred to a 10 cm  
463 dish containing 20 ml liver digest medium. The liver was dissected allowing the cells to  
464 spill into the media. The cells were then filtered through a 40 µm cell strainer into a 50  
465 ml tube and 30 ml media (Williams E media + 2 µg/ml human insulin + 1x glutamax +  
466 10% FBS) were added and placed on ice. The hepatocytes were purified by  
467 centrifugation at 50 x G, 4 times for 3 minutes each, each time discarding the  
468 supernatant and adding media.

469

470 **Single cell RNA sequencing.**

471 Single-cell RNA sequencing was performed as previously described<sup>4,5</sup> with the following  
472 modifications. In this study, we used small (5-10 µm), medium (10-17 µm), and large

473 (17-25  $\mu$ m) plate sizes. ERCC RNA Spike-In (ThermoFisher Cat. No. 4456740) was  
474 diluted in the lysis mix following the manufacturer's user guide and previous studies<sup>36</sup>.  
475 Single end reads of 51 bp were sequenced on an Illumina HiSeq 2500 system.  
476 Sequencer outputs were processed using Illumina's CASAVA-1.8.2. The demultiplexed  
477 reads were trimmed and filtered to eliminate adapter sequence and low-quality  
478 basecalls. The reads were mapped to an mm10 mRNA transcript reference (extended  
479 with ERCC transcripts) using bowtie-0.12.9<sup>37</sup>; expression estimates were generated  
480 using RSEM v.1.2.3<sup>38</sup>.

481 Using the Fluidigm C1 system to capture and synthesize cDNA from single cells in the  
482 liver, we generated transcriptomes for 149 cells. To exclude low quality transcriptomes,  
483 we removed cells in which the fraction of ERCC spike-in made up 20% or more of the  
484 total assigned reads. This left 66 high quality cells, that were used in the downstream  
485 analysis. Finally, the data was normalized using SCnorm (R package v 1.5.7)<sup>39</sup>.

486

487 **Data availability.**

488 scRNA-sequencing data that support the findings of this study have been deposited in  
489 NCBI's Gene Expression Omnibus with the GEO Series accession code "GSE116140"  
490 <https://www.ncbi.nlm.nih.gov/geo/query/acc.cgi?acc=GSE116140>. The normalized and  
491 ordered expression data is provided as Additional File 4.

492 All code used in the analysis and figures is available on Github at  
493 <https://github.com/rhondabacher/LiverSpatialCompare>.

494

495 **Pseudo-spatial reordering.**

496 For the full-length data, the cells were computationally ordered using the Wave-Crest  
497 method as described by Chu et al. 2016<sup>5</sup>. Prior to reordering, gene expression values  
498 were rescaled to mean 0 and variance 1 to ensure the values across different genes are  
499 comparable. The Wave-Crest algorithm implements an extended nearest insertion  
500 algorithm that iteratively adds cells to the order and selects the insertion location as the  
501 location producing the smallest mean squared error in a linear regression of the  
502 proposed order versus gene expression. A 2-opt algorithm is then used to find an  
503 optimal cell order by considering adjacent cell exchanges. The cell ordering step uses  
504 the expression profiles of pre-selected known marker genes of liver zonation. Thus, the  
505 resulting linear profile of ordered cells represents the periportal to pericentral axis. The  
506 known marker genes used to construct the periportal to pericentral axis in Wave-Crest  
507 include the following pericentral markers: cytochrome P450 7a1 (Cyp7a1), cytochrome  
508 P450 2e1 (Cyp2e1), ornithine aminotransferase (Oat), cytochrome P450 1a2 (Cyp1a2),  
509 rh family, B glycoprotein (Rhbg), leucine-rich repeat-containing G-protein coupled  
510 receptor 5 (Lgr5), glutamate-ammonia ligase (Glul); and the following periportal  
511 markers: phosphoenolpyruvate carboxykinase 1 (Pck1), catenin beta interacting protein  
512 1 (Ctnnbip1), aldehyde dehydrogenase 1 family member B1 (Aldh1b1), sulfotransferase  
513 family 5A, member 1 (Sult5a1), cytochrome P450 2f2 (Cyp2f2), cathepsin C (Ctsc),  
514 serine dehydratase (Sds), and E-cadherin (Cdh1). All markers were selected based on  
515 their expression ratio as reported by Braeuning et al. 2006<sup>21</sup>.  
516  
517 A detection step was done to identify additional genes that follow the one-dimensional  
518 periportal to pericentral axis by fitting a linear regression to the relationship between

519 each gene's expression and the Wave-Crest cell order. To determine if a gene is  
520 significantly dynamic (zonated) along the recovered axis, we tested whether the  
521 regression slope is different from zero. We reported the Benjamini-Hochberg adjusted  
522 p-values to control the false discovery rate. For genes having an adjusted p-value < .01,  
523 the direction of the expression profile was assigned based on the sign of the regression  
524 slope (periportal: positive slope, pericentral: negative slope). We also calculated the  
525 linear fitting mean squared error (MSE) for each significant gene. Genes with a  
526 smoother trend over the recovered cell order are expected to have a smaller MSE. We  
527 reported the full list of significant genes, sorted by their MSE, in Additional File 2; scatter  
528 plots are shown in Additional File 3.

529

### 530 **Comparative Analysis**

531 Smoothed densities (bean plots) with overlaid raw data, the mean, and a box  
532 representing the interquartile range of the cellular detection fractions were created using  
533 the pirateplot function in the yarrr R package (v0.1.5). The cellular detection fraction  
534 was calculated per cell as the proportion of genes having expression greater than zero.  
535 The fold-change for each gene between the two datasets was calculated as the log2  
536 fold-change of the full-length gene mean over the UMI gene mean, where each gene  
537 mean was calculated as the average expression among non-zero counts across all cells  
538 in the datasets. The heatmap in Figure 2 of marker gene expression on the normalized  
539 Smart-seq data was generated by setting values above the 95th percentile or below the  
540 5nd percentile to the 95th percentile or 5nd percentile value, respectively

541

542 When comparing the two datasets having different dynamic ranges, we used scaled  
543 expression plots, where the ordered cells in the full-length dataset were divided into  
544 nine equally sized groups to correspond to the nine layers in the UMI dataset. For the  
545 full-length dataset, for a given gene, the median expression in each group was  
546 calculated, then the nine means were scaled between zero and one. Smoothed fits  
547 were overlaid using the smooth.spline function in R with the degrees of freedom  
548 parameter df=4. Expression correlations along the zonation axis between datasets were  
549 calculated using Spearman correlation. Enrichment of genes in KEGG pathways or GO  
550 was done using the R package clusterProfiler (v. 3.10.1)<sup>40</sup>. For the enrichment analysis,  
551 since different statistical methods were used to assess zonation profiles, genes were  
552 considered significantly zonated if they had an adjusted p-value < .1 in both datasets  
553 and more than 10 non-zero expression values. The heatmap in Figure 3 is a smoothed  
554 heatmap, where a smoothing spline was first fit to the log expression (pseudo-count of  
555 one added) of each gene using the smooth.spline function in R with the smoothing  
556 parameter df=4 which provided profiles that were not over- or underfit in either dataset.  
557 Then the smoothed expression was scaled and outliers above the 98<sup>th</sup> percentile or  
558 below the 2<sup>nd</sup> percentile were set to the 98<sup>th</sup> percentile or 2<sup>nd</sup> percentile value,  
559 respectively. Additional KEGG categories from this analysis can be interactively viewed  
560 on Github <https://github.com/rhondabacher/LiverSpatialCompare>.

561

## 562 **Subsampling Analysis**

563 In all subsamplings described below, each scenario was repeated a total of 25 times  
564 and the zonation group means were scaled to be between zero and one.

565

566 For the MARS-seq dataset, zonation group means were recalculated on a subsampled  
567 set of cells using the posterior probability matrix and original UMI counts from Halpern  
568 et al. 2017. In each sampling, the mean squared error (MSE) was calculated based on a  
569 random sample of 500 genes as  $\sum_{i=1}^{500} \sum_{j=1}^9 (Z_{i,j} - \hat{Z}_{i,j})^2 / 500$ , where  $Z_{i,j}$  represents the  
570 mean expression of gene  $i$  in zonation group  $j$  in the original dataset and  $\hat{Z}_{i,j}$  is the  
571 corresponding value for the subsampled dataset. For subsampling at lower read depths,  
572 we fixed the number of cells at the original total of 1415 cells and simulated each cell's  
573 gene counts individually using a multinomial distribution. For each cell, the subsampled  
574 total counts were set to  $X\%$  of the original total read counts for that cell (for  $X =$   
575 (10,20,30,40,50,60,70,80,90,100)) and each gene's cell-specific probability was  
576 calculated as its original count divided by the original total counts for that cell. The MSE  
577 was calculated for each subsampled set as described above.

578

579 For the Smart-seq dataset, we reran Wave-Crest when subsampling the total number of  
580 cells using the original parameter settings and marker genes. Then, as before, the  
581 ordered cells were assigned zonation groups by dividing cells into nine equally sized  
582 groups. The zonation profile error was estimated using MSE and calculated as  
583 described above with the exception that since Wave-Crest orders can be flipped, we  
584 calculated the MSE on the returned order and its reverse, and kept the minimum MSE  
585 of the two. We also computed the MSE similarly on random permuted orders of the full  
586 66 cells to assess the maximal MSE distribution. For evaluating lower read depths, we  
587 first determined the effect of lower read depth on the ordering accuracy by re-running

588 Wave-Crest on lower read-depth subsampled datasets and calculating the correlation of  
589 the original order to the cell order obtained on the subsampled data. To evaluate the  
590 zonation profile error with lower read depths, we used a similar approach as described  
591 above for the MARS-seq dataset, fixing the number of cells to be the same as the  
592 original total of 66 and, since the order correlation was shown to be consistently high,  
593 we used the original Wave-Crest order for every scenario when evaluating zonation  
594 profile error.

595 **Immunohistochemistry.**

596 An 8-week-old male C57BL/6 mouse was anesthetized using isoflurane before  
597 euthanizing by cervical dislocation. The liver was excised, sliced as thinly as possible  
598 with a razor blade, and fixed in formaldehyde overnight. The liver slices were paraffin  
599 embedded and sectioned. Sections were stained following the protocol published by  
600 Abcam ([http://www.abcam.com/ps/pdf/protocols/ihc\\_p.pdf](http://www.abcam.com/ps/pdf/protocols/ihc_p.pdf)). In short, the slices are  
601 deparaffinized by dipping into sequential solutions of 100% xylene, 50-50% xylene-  
602 ethanol, 100% ethanol, 95% ethanol, 70% ethanol, 50% ethanol, and tap water. The  
603 antigens were then retrieved by placing the slides in Tris-EDTA buffer (10 mM Tris  
604 Base, 1 mM EDTA Solution, 0.05% Tween 20, pH 9.0) and incubating them in a  
605 decloaking chamber (Biocare Medical Decloaking Chamber #DC2008US) with the  
606 following settings: delayed start 30 sec.; preheat 80°C, 2 min.; heat 101°C, 3 min. 30  
607 sec.; and fan on. The slides were washed 2 x 5 min in TBS + 0.025% Triton X-100  
608 before they were blocked for two hours at room temperature in 10% normal serum in  
609 1% BSA. The appropriate primary antibody was then diluted in the same 10% normal  
610 serum in 1% BSA, added to the slides, and incubated at 4°C overnight in an incubation

611 chamber. The next day the slides were washed 2 x 5 min in TBS + 0.025% Triton X-100  
612 followed by 15 min incubation in 0.3% H<sub>2</sub>O<sub>2</sub> at room temperature. Next, the appropriate  
613 secondary antibody was diluted into 10% normal serum in 1% BSA before it was added  
614 to the slides and incubated for 1 hour at room temperature. The slides were then  
615 washed 3 x 5 min in TBS before DAB (#ab103723) staining mixed according to  
616 manufacturer instruction was applied and incubated under a microscope to stop the  
617 reaction after sufficient staining. The slides were rinsed in tap water for 5 min before  
618 being counterstained with Mayer's hematoxylin (#MHS1-100ML) for 30 sec. The stain  
619 was developed in running tap water for 5 min. The slides were then dehydrated by  
620 sequentially dipping in 50% ethanol, 70% ethanol, 95% ethanol, 100% ethanol, 50-50%  
621 xylene-ethanol, and 100% xylene before Poly-Mount (#08381-120) was added and a  
622 coverslip placed on top. The following primary antibodies were added: Aldh3a4 1:250  
623 (AB184171), Cyp2e1 1:50 (AB28146), Cyp1a2 1:50 (R31007), Rgn 1:100 (NBP1-  
624 80849), Oat 1:50 (AB137679), Cyp2f2 1:100 (SC-67283), Hal 1:50 (AV45694), and  
625 Tbx3 1:50 (SC-31657). The following secondary antibodies were used: goat-anti-rabbit  
626 HRP conjugated (ab97051) and donkey-anti-goat HRP conjugated (ab97110) at a  
627 concentration of 1:500.

628

## 629 **Additional Files**

630 Additional File 1 – Supplementary Figures and Tables.  
631 Additional File 2 – Summary of genes with dynamic expression across the zonation axis  
632 identified using Wave-Crest.  
633 Additional File 3 – Scatter plots of dynamic genes listed in Additional File 2.

634 Additional File 4 – Normalized Smart-Seq single-cell data with cells in the Wave-Crest  
635 order.